

Main Manuscript for

A mixed valent Fe(II)Fe(III) species converts cysteine to an oxazolone/thioamide pair in methanobactin biosynthesis

Yun Ji Park,^a Richard J. Jodts,^a Jeffrey W. Slater,^b Reyvin M. Reyes,^a Valerie J. Winton,^a Rana A. Montaser,^a Paul M. Thomas,^a William B. Dowdle,^a Anahi Ruiz, ^a Neil L. Kelleher,^a J. Martin Bollinger, Jr.,^b Carsten Krebs,^b Brian M. Hoffman,^a and Amy C. Rosenzweig*
^aDepartments of Molecular Biosciences and Chemistry, Northwestern University, Evanston IL 60208, USA

^bDepartment of Chemistry and Department of Biochemistry and Molecular Biology, The Pennsylvania State University, University Park, PA 16802, USA.

*Amy C. Rosenzweig

Email: amyr@northwestern.edu

Author Contributions: Y.P., R.J.J., J.W.S, R.M.R., V.J.W, C.K., J.M.B., B.M.H., and A.C.R. designed research. Y.P., R.J.J., J.W.S, R.M.R., V.J.W, R.A.M, W.B.D, and A.R performed research. Y.P., R.J.J., J.W.S, R.M.R., V.J.W, P.M.T., and C.K analyzed data. Y.P., R.J.J., J.W.S., R.M.R., V.J.W., R.A.M, N.L.K., C.K., J.M.B., B.M.H., and A.C.R. contributed to the manuscript.

Competing Interest Statement: The authors declare no competing interest.

Classification: BIOLOGICAL SCIENCES, Biochemistry

Keywords: MbnBC, methanobactin, nonheme iron, natural products biosynthesis

This PDF file includes:

Main Text Figures 1 to 8

Abstract

The iron-containing heterodimeric MbnBC enzyme complex plays a central role in the biosynthesis of methanobactins (Mbns), ribosomally-produced, post-translationally modified natural products that bind copper with high affinity. MbnBC catalyzes a four-electron oxidation of a cysteine residue in its precursor-peptide substrate, MbnA, to an oxazolone ring and adjacent thioamide group. Initial studies of MbnBC indicated the presence of both diiron and triiron species, complicating identification of the catalytically-active species. Here we present evidence through activity assays combined with electron paramagnetic resonance (EPR) and Mössbauer spectroscopic analysis that the active species is a mixed valent, antiferromagnetically coupled Fe(II)Fe(III) center. Consistent with this assignment, heterologous expression of the MbnBC complex in culture medium containing less iron yielded purified protein with less bound iron but greater activity in vitro, and the maximally activated MbnBC prepared in this manner could modify both cysteine residues in MbnA. in contrast to prior findings that only the first cysteine could be processed. Site-directed mutagenesis combined with multiple crystal structures clearly identifies the two essential Fe ions in the active cluster as well as the location of the previously detected third Fe site. Moreover, structural modeling indicates a role for MbnC in recognition of the MbnA leader peptide. These results add an unprecedented biosynthetic oxidative rearrangement reaction to the repertoire of nonheme diiron enzymes and provide a foundation for elucidating the MbnBC mechanism.

Significance Statement

Methanobactins, copper-binding peptidic compounds produced by some types of bacteria, are candidate therapeutics for human diseases of copper overload. The paired oxazolone-thioamide bidentate ligands of methanobactins are generated from cysteine residues in a precursor peptide, MbnA, by the MbnBC enzyme complex. MbnBC activity depends on the presence of iron, but the catalytically-active form has not been identified. Here we provide evidence that a dinuclear Fe(II)Fe(III) center in MbnB, which is the only representative of a >13,000 member protein family to be characterized, is responsible for this reaction. These findings expand the known roles of diiron enzymes in biology and set the stage for mechanistic understanding, and ultimately, engineering, of the MbnBC biosynthetic complex.

Main Text

Introduction

The MbnBC enzyme complex is central to the biosynthesis of methanobactins (Mbns), copper-binding metallophores isolated from methane-oxidizing (methanotrophic) bacteria and currently under investigation as therapeutics for Wilson disease (1, 2). Mbns are ribosomally produced, post-translationally modified peptide (RiPP) natural products generated from a precursor peptide, MbnA (3). Operons encoding MbnA along with the Mbn biosynthetic and transport machinery are found in a range of bacteria besides methanotrophs and are predicted to yield a diverse array of natural products (4). Mbns chelate copper with high affinity by using two nitrogen and two sulfur atoms derived from nitrogen-containing heterocycles and neighboring thioamide groups (Fig. S1) (5-10). These paired oxazolone ring and thioamide groups, present in all Mbns characterized thus far, are generated from two conserved cysteine residues and the carbonyl groups of their preceding residues (Fig. 1A) by two proteins, MbnB and MbnC, which form a heterodimeric complex denoted MbnBC (11). In a subset of Mbns, one nitrogen ligand is provided by a pyrazinedione ring proposed to result from further modification of an oxazolone ring originally produced by MbnBC (Fig. S1) (7, 10). While additional modifications occur in the biosynthesis of some Mbns, MbnBC is universally present in the operons and is thus the linchpin of this pathway.

MbnB is the only biochemically characterized member of the DUF692 protein family, which includes >13,000 sequences (UniProt), while MbnC belongs to a completely uncharacterized

protein family (11). Initial studies showed that MbnBC requires both Fe and O₂ to convert cysteine into an oxazolone/thioamide pair (Fig. 1*A*). According to top-down native mass spectrometry (nTDMS) measurements, MbnB ejected from the MbnBC complex contains three Fe ions. Mössbauer spectroscopic analysis further indicated that MbnBC contains a mixture of triferric [Fe(III)]₃ and diferric [Fe(III)]₂ clusters, and model of MbnBC based on the unpublished crystal structure of a diiron center-containing homolog from *Haemophilus somnus* 129pt (PDB accession code 3BWW) suggested possible ligand sets for three Fe ions (Fig. 1*B*) (11). Variants in which predicted ligands His54, His90, Glu133, Asp163, His192, and Glu239 were individually replaced with alanine or serine (Fig. 1*B*) exhibited diminished Fe content and significantly less cysteine modification activity, supporting a functional role for Fe coordinated by these residues (11).

Despite these advances, heterogeneity in the MbnBC Fe site, as evidenced by the observation of both dinuclear Fe₂(III) and trinuclear Fe₃(III) clusters by Mössbauer spectroscopy, has complicated identification of the catalytically active species. Moreover, modification of only the first, but not the second, modifiable cysteine in MbnA was reported previously (11), suggesting that the enzyme was not fully activated. The involvement of an Fe-containing enzyme in oxazolone and thioamide synthesis is unique, and establishing the nuclearity and redox state of the active species is critical to understanding the mechanism. Here we provide evidence through electron paramagnetic resonance (EPR) and Mössbauer spectroscopies combined with enzymatic activity assays, crystal structures, and mass spectrometric analysis that the active species of MbnBC is a mixed-valent Fe(II)Fe(III) cluster coordinated by conserved residues in MbnB. These findings set the stage for detailed mechanistic studies and expand the diversity of reactions attributable to nonheme diiron enzymes in natural product biosynthesis.

Results and Discussion

MbnB activity derives from a mixed-valent diiron Fe(II)Fe(III) cluster. To identify the Fe species that reacts with MbnA and O₂, EPR, Mössbauer, and activity data were acquired for MbnBC samples in various Fe oxidation states. Methylosinus (Ms.) trichosporium OB3b MbnBC was heterologously expressed in *E. coli* in the presence of 250 µM supplemental ⁵⁷Fe and purified using established protocols (11). The resultant protein was first treated with ferricyanide to generate a fully oxidized (all ferric) sample (oxMbnBC). The EPR spectrum of this sample (Fig. 2A, oxMbnBC + 0.0 eq. asc) exhibits a strong signal at $g_{\rm eff}$ = 4.3 and several weaker signals with $g_{\rm eff}$ -values of ~ 8.5, 6.9, 4.9, characteristic of "rhombic" S = 5/2 Fe(III). In addition, there is a weak signal at g < 2attributable to the S = 1/2 ground state of an antiferromagnetically coupled Fe(II)Fe(III) cluster (Fig. 2A); double integration of this signal reveals the presence of 9 µM Fe(II) Fe(III) clusters (~1% of the total Fe in the sample). This spectrum of oxMbnBC is nearly the same as that obtained for aerobically purified MbnBC, but lacks features previously observed above 4000 Gauss (11). The Mössbauer spectrum of oxMbnBC (Fig. 2B) is similar to that published previously (11) (Fig. S2) and exhibits the broad magnetically split features associated with an Fe₃(III) cluster (blue arrows) and/or adventitiously bound high-spin Fe(III) (blue arrows), in addition to a quadrupole doublet with parameters reported for that of the Fe₂(III) cluster (red line, ~20% of total intensity).

Treatment of oxMbnBC with ascorbate (redMbnBC_asc) results in marked changes to the EPR spectrum. First, a rhombic EPR signal with $g = [1.94, 1.88, 1.76, g_{ave} = \sim 1.9]$ is observed and is well resolved at ~10-30 K (Fig. 2A). This signature is attributed to an antiferromagnetically coupled Fe(II)Fe(III) cluster with an S = 1/2 ground state, a unit that has been characterized extensively in both diiron enzymes and synthetic model complexes thereof (12-14). The intensity of the S = 1/2 EPR signal reached maximum upon the addition of 1-2 equiv of ascorbate (Fig. 2A), integrated to ~80 µM spin, and persisted upon addition of 5 equiv of ascorbate, indicating that ascorbate cannot lead to efficient reduction of the cluster (Fig. S3). The ~80 µM spin of the Fe(II)Fe(III) species accounts for 13% of the total iron in the sample, or 66% of the Fe₂(III) deduced from the Mössbauer spectrum of the fully oxidized sample (Fig. 2B). Addition of 2 equiv of dithionite (redMbnBC_dt), however, results in a decrease of the intensity of the S = 1/2 signal, suggesting further reduction to an Fe₂(II) cluster (Fig. 2A). In addition, the pronounced signal at $g_{eff} = 4.3$ is reduced ~5-fold in intensity and the low-field signals disappear completely, suggesting that the majority of the S = 5/2 rhombic Fe(III) is reduced. A new, broad signal extending from g = 4.5 to g = 1/2 signal extending from g = 4.5 to g = 1/2 signal extending from g = 4.5 to g = 1/2 signal extending from g = 4.5 to g = 1/2 signal extending from g = 4.5 to g = 1/2 signal extending from g = 4.5 to g = 1/2 signal extending from g = 4.5 to g = 1/2 signal extending from g = 4.5 to g = 1/2 signal extending from g = 4.5 to g = 1/2 signal extending from g = 4.5 to g = 1/2 signal extending from g = 1/2 signal extending from

= 6.7 appears as well, and could derive from an alteration in the zero-field splitting of residual highspin Fe(III) or from a 2e⁻ reduced Fe₂(II)/Fe(III) cluster.

The Mössbauer spectrum of a sample of oxMbnBC treated with 1 equiv of ascorbate (Fig. 2B, vertical bar) exhibits broad, relatively featureless absorption, extending from ~-7 mm/s to ~+7 mm/s, revealing that the majority of the Fe exhibits magnetically split features. Most notably, the broad quadrupole doublet associated with the Fe₂(III) cluster is diminished in intensity (Fig. 2C), consistent with the appearance of the EPR signal associated with the S = 1/2 Fe(II) Fe(III) cluster. This species is expected to exhibit magnetically split subspectra, but accounts for only ~12% of the total intensity of the spectrum (80 μM spin × 2 Fe per dinuclear cluster / 1.3 mM total Fe). Moreover. because the low field EPR features are diminished significantly by ascorbate treatment, the majority of the broad, magnetically split features must arise from another Fe species. One candidate for this species is a 1e⁻-reduced trinuclear cluster, Fe(II)Fe₂(III), which would have an integer spin ground state that could give rise to magnetically split spectra (although the majority of integer-spin clusters exhibit quadrupole doublet features under these conditions). Alternatively, this species could be a 2e⁻-reduced trinuclear cluster, Fe₂(II)Fe(III), which has a half-integer spin ground state and is expected to exhibit magnetically split Mössbauer spectra, the presence of which could be inferred from the broad EPR signals at g = 5-6. We have not further analyzed these spectra, due to their lack of resolution and the fact that the broad component is a superposition of multiple subspectra.

MbnBC samples in each of the three oxidation states, oxMbnBC (Fig. 3A), redMbnBC_asc prepared with 2 equiv of ascorbate (Fig. 3B), and redMbnBC_dt (Fig. 3C), were then tested for MbnA modification activity. For each assay, MbnBC prepared in the anaerobic chamber was mixed with an equal volume of MbnA in air-saturated buffer using a stopped-flow apparatus, and MbnA modification was monitored by the appearance of an optical feature at 335 nm, arising from the oxazolone ring (11). A comparison of the kinetic traces indicates that redMbnBC_asc produces the modified MbnA product with the greatest initial velocity and yield at completion (Fig. 3D).

Given that redMbnBC_asc gave the highest rate and extent of MbnA modification, 2 equiv MbnA were added to redMbnBC_asc under anaerobic conditions to generate the reactant complex, and the effects of substrate binding on different Fe species was examined by EPR and Mössbauer spectroscopies. In the EPR spectrum, the S = 1/2 $g_{ave} \sim 1.9$ feature attributed to the antiferromagnetically coupled Fe(II)Fe(III) center is converted to a new, sharper feature with g-values of 1.92, 1.89, 1.82 (Fig. 4). The perturbation suggests that MbnA binding modifies the coordination sphere of the Fe(II)Fe(III) cluster. Indeed, similar perturbations upon addition of substrate have been observed for all three HD-domain mixed-valent diiron oxygenases and oxidases (MVDOs) that have been studied to date (15-17). The residual $g = \sim 5.8$ signal also is perturbed upon substrate addition (Fig. S4). The Mössbauer spectrum of redMbnBC_asc in the presence of MbnA (Fig. S5) is consistent with this assignment.

To further correlate activity with the prevalence of the Fe(II)Fe(III) cluster, catalytically-impaired variants in which the proposed Fe ligands were replaced with alanine or serine (H54A, H90S, E133A, D163S, H192A, and E239A) (Fig. 1B) (11), were isolated, treated with 2 equiv ascorbate, and examined by EPR spectroscopy (Fig. S6). With the exception of D163S, these substitutions abolished the signals from the Fe(II)Fe(III) cluster, consistent with a first coordination sphere including H54, H90, E133, H192, and E239. The D163S substitution changed, but did not abolish, the Fe(II)(III) EPR signal, consistent with this residue as a weakly interacting ligand.

Low Fe MbnBC produces a higher yield of modified MbnA. The correlation between activity and the presence of a Fe(II)Fe(III) cluster combined with the observation of both Fe₂(III) and Fe₃(III) clusters by Mössbauer spectroscopy and nTDMS (11) suggested that our MbnBC sample preparation could be improved to maximize the amount of active Fe(II)Fe(III) species. We therefore tried to prepare an MbnBC sample with a homogeneous Fe₂(III) cluster. Initial attempts to remove Fe from MbnBC using ferrozine, which significantly diminishes activity (11), and to reload with either Fe(II) or Fe(III) were unsuccessful. As an alternative approach, MbnBC was heterologously expressed in *E. coli* with less Fe in the growth medium (160 μ M compared to 250 μ M used above and >250 μ M used in prior work (11)). Inductively coupled plasma mass spectrometry (ICP-MS) measurements indicated that the MbnBC isolated from these cultures

(MbnBC_{lowFe}) contained 0.82 ± 0.02 equiv of Fe, whereas MbnBC isolated from cultures with 250 μ M Fe (MbnBC_{highFe}, used for above experiments) contained 1.05 ± 0.2 equiv Fe.

The enzymatic activities of MbnBC_{lowFe} and MbnBC_{highFe} were then compared. The samples were first treated with 2 equiv of ascorbate to maximize the presence of the Fe(II)Fe(III) species (redMbnBC_{lowFe}_asc, redMbnBC_{highFe}_asc). Activity assays were then initiated by adding 1.3 equiv of the substrate MbnA to ascorbate-treated MbnBC under ambient aerobic conditions to provide excess O₂ to the reaction as a cosubstrate. Strikingly, the reaction with redMbnBC_{lowFe}_asc (Fig. 5A) yielded significantly more product (~1.8x) than the reaction with MbnBC_{highFe} asc (Fig. 5B).

To discern the differences between the MbnBC_{highFe} and MbnBC_{lowFe} samples, MbnBC_{lowFe} was examined by EPR and Mössbauer spectroscopies. The Mössbauer spectrum of oxMbnBlowFe reveals an increased intensity of the quadrupole doublet associated with the Fe₂(III) cluster, 32% in oxMbnBC_{lowFe} vs 20% in oxMbnBC_{highFe} (Fig. 5C, Fig. S7). The remainder of the absorption comprises the broad, magnetically split features associated with the Fe₃(III) cluster and/or adventitiously bound high spin Fe(III). Upon reduction with ascorbate, the Mössbauer spectrum shows a decrease in intensity of the quadrupole doublet from the Fe₂(III) state and an increased intensity of the magnetically split features, in addition to a new line at ~+3 mm/s, which is assigned as the high energy line of high spin Fe(II) generated from reduction of adventitiously bound high spin Fe(III) (Fig. 5C). The EPR spectra of redMbnBClowFe_asc are similar to those of MbnBC_{highFe_}asc, exhibiting identical features at g = 1.8 and $g_{eff} = 4.3$, of which the latter signal likely derives from underloaded diiron cluster (Fig. S8A). The signal at S = 1/2 with $g_{ave} \sim 1.9$ integrates to ~35 µM spin, which corresponds to ~19% of total Fe and ~60% reduction yield of Fe₂III, which is consistent with the yield observed for MbnBC_{highFe}. The activity profiles of MbnBC_{low} in the three oxidation states (Fig. S8B) recapitulate those of MbnBChighFe (Fig. 3). The lesser quantity of Fe₃(III) cluster in the highest activity redMbnBC_{lowFe} asc sample further supports the identification of the MbnBC active species as a mixed-valent Fe(II)Fe(III) cluster.

Crystal structure of MbnBC reveals three Fe binding sites. To confirm the proposed ligand set for the Fe(II)Fe(III) cluster and assess the presence and importance of the third Fe ion detected by Mössbauer spectroscopy and nTDMS (11), we determined the crystal structure of MbnBC. Initial attempts to grow crystals of wildtype Ms. trichosporium OB3b MbnBC did not yield diffracting crystals. The crystal quality was improved significantly by removal of 8 predicted disordered residues from the MbnB C-terminus and mutagenesis of predicted surface patches guided by the Surface Entropy Reduction prediction (SERp) server (MbnB E67A, E69A, K70A, MbnC E162A, E164A, K165A) (18). The structure of MbnBC expressed with 250 μ M Fe was solved to 2.6 Å resolution by Fe single wavelength anomalous dispersion (SAD), and additional structures of MbnBC expressed with 80 μ M Fe, the H210S variant, and MbnBC crystallized anaerobically in the presence of the core peptide were determined by molecular replacement (Table S1).

As predicted, MbnB exhibits an 8-stranded TIM-barrel fold (Fig. 6A), and closely resembles the *Haemophilus somnus* 129pt DUF692 protein (PDB accession code 3BWW), with an rmsd of 3.8 Å for superposition of 224 C α atoms. Three loop regions that were unmodeled in the *Haemophilus somnus* 129pt protein are well ordered in MbnB (Fig. S9A). MbnC caps the MbnB TIM barrel, leaving a large open cavity above the iron site (Fig. 6A), presumably for MbnA binding. There are numerous intersubunit interactions, with 2113 Ų buried surface area at the protein-protein interface (calculated using the PDBePISA server). MbnC consists of an N-terminal α -helical domain and two additional α helices packed against a 4-stranded antiparallel β sheet (Fig. 6A). The MbnC fold does not resemble any previously characterized protein. A search of the Dali server yielded a partial structural match to a member of Pfam family PF09836 from *Neisseria gonorrhoeae* (PDB accession code 3DEE) (Fig. S9B). Interestingly, this protein, proposed to play a role in transcriptional regulation, also neighbors a member of the DUF692 family (19). The MbnC surface housing the three surface entropy reduction substitutions, E162A, E164A, K165A, forms an antiparallel β -strand interaction with a symmetry-related molecule, explaining why this crystallization strategy was successful (Fig. S10).

Anomalous electron density maps calculated using data collected at the Fe absorption edge yield two strong peaks (37σ) , modeled as Fe ions (Fig. 6B). The two Fe ions are six-coordinate, bridged by Glu133, along with two exogenous ligands modeled as a solvent molecule

and a sulfate ion, analogous to the cacodylate ion in the Haemophilus somnus 129pt homolog structure and likely derived from the LiSO₄ used for crystallization. Fe1 is further coordinated by the ϵ nitrogen atoms of His54 and His90 and a solvent molecule while Fe2 is coordinated by δ nitrogen atom of His192 and by one carboxylate oxygen each from Asp163 and Glu239 (Fig. 6B, Fig. S11A). Given that activity (11) and the Fe(II)Fe(III) EPR signal (Fig. S6) are disrupted upon replacement of these residues, these two Fe ions can be assigned as the active cofactor of MbnBC. A third peak (5σ) is also present in the anomalous electron density map, located between residues Asp208 and His210 at the proposed location of the third Fe ion (Fig. 1). The density is much weaker than that for Fe1 and Fe2, but was best modeled as an Fe ion at occupancies of 0.52 and 0.65 in the two molecules in the asymmetric unit. This Fe ion, designated Fe3, is coordinated by the ϵ nitrogen of His210 and the side chain oxygen of Asn166 (Fig. 6B, Fig. S11A), which was not anticipated as a ligand, but is highly conserved. Proposed ligand Asp208 (Fig. 1) is disordered, likely due to partial Fe occupancy of this site. A second structure of MbnBC, determined to 2.3 Å resolution (Table S1) using protein expressed in the presence of 80 μM rather than 250 μM Fe, showed even lower occupancy of the third Fe site (0.4 in both subunits) and no evidence for the bridging sulfate ion. Instead, Fe1 and Fe2 are each coordinated by an additional terminal solvent molecule (Fig. S11B).

Extensive attempts at cocrystallization with full length MbnA were not successful, but a 2.2 Å resolution structure was determined from crystals grown anaerobically in the presence of 10 equiv MbnA core peptide. Interestingly, anomalous electron density maps for this structure showed full occupancy of all three Fe sites (30-35 σ) (Fig. 6C). In this structure, Asp208 adopts a new position, coordinating directly to Fe3, which is also coordinated by Asn166 and His210 (Fig. 6C, Fig. S11C). Given that MbnBC used for this structure was also expressed in the presence of 250 μ M Fe, it is not clear why full occupancy of Fe3 is achieved. No density corresponding to the core peptide was apparent, and additional structures determined from crystals grown anaerobically in the absence of core peptide gave identical structures with all three Fe sites fully occupied.

In the absence of a co-crystal structure with MbnA, we used Alphafold2 (20) as accessed through ColabFold (21) to generate a model of the MbnABC complex (Fig. S12). In this model structure, modifiable Cys21 of MbnA is positioned adjacent to Fe1, supporting the assignment of an Fe(II)Fe(III) cluster comprising Fe1 and Fe2 as the active cofactor. Strikingly, residues 6-11 of the MbnA leader peptide form an extended β sheet with 4-stranded antiparallel β sheet of MbnC, interacting with MbnC residues 158-162 (Fig. S12). This interaction resembles a common leader peptide recognition element involving the formation of an extended beta-sheet between a helix-turn-helix motif of a biosynthetic enzyme and its substrate (22, 23). This interface also explains why cocrystallization of MbnBC with MbnA was not successful; MbnC residues 158-162 interact closely with a symmetry-related molecule in the crystal lattice (Fig. S10).

MS² analysis shows that both MbnA modifiable cysteine residues are converted to oxazolone/thioamide groups. Having identified the active species and optimized the conditions for MbnBC activity, we analyzed the final product of the reaction between redMbnBC_{lowFe}_asc and MbnA by liquid chromatography-tandem mass spectrometry (LC-MS/MS). In the MS¹ chromatogram, two related species were observed with a mass difference corresponding to 2 protons (2.02 Da), suggesting the presence of disulfide bond in one of the species. The triply charged ions of species A presented a monoisotopic peak at 1065.154 m/z, which corresponds to a mass of 3192.42 Da. The m/z of the monoisotopic peak for species B was 1065.826, deconvoluting to a mass of 3194.46 Da (Fig. 7, Fig. S13). These parental masses from MS¹ are consistent with the mass of MbnA in which two cysteine residues are modified to an oxazolone ring and a thioamide group along with the binding of one Cu (Fig. 7).

To localize specific modifications, both species were targeted for MS^2 fragmentation experiments. In species A (disulfide bond intact) fragmentation localizes the loss of 4H to Cys_{21} , consistent with its modification to an oxazolone/thioamide group (Fig. 7). Because there is no further fragmentation between Cys_{24} and Cys_{29} , the second cysteine modification could not be localized in species A, possibly due to the presence of the disulfide bond. Notably, all y-type fragment ions bind Cu (Fig. 7, fragments shown in purple) and some of the smaller fragments, including y_7 , y_8 , and y_9 , show an isotopic pattern consistent with the presence of ^{63}Cu and ^{65}Cu

(Fig. S14), supporting the identification of the Cu-bound form of the product. Extra Cu was not added to the sample, suggesting that modified MbnA binds trace Cu from the environment.

In MS² fragmentation experiments of species B (reduced disulfide bond), the Cu ion was not present (presumably lost during the MS² experiment), and more fragment ions were detected. Two fragment ions, which were not obtained for species A, y₂ and y₃, contain Cys₂₃ and show no modification thereof, suggesting that the second modification, corresponding to a loss of 5H, is localized on Cys₂₁ (Fig. 7). The loss of a proton compared to Cys₂₁ (-4H) is likely due to deprotonation of the –SH group upon Cu binding. Modification at Cys₂₁ is consistent with the structure of *Ms. trichosporium* OB3b Mbn and the presence of conserved modification motifs (4, 6, 24). Thus, the MS² analysis shows that the optimized reaction conditions result in modification of both cysteine residues in the MbnA precursor peptide, and that cleavage of the leader peptide is not required for Cys₂₁ modification as proposed previously (11). Although MbnBC is sufficient to modify both cysteine residues, prior work showed that Cys₂₁ is required for any modification to occur (11). Exactly how MbnBC recognizes MbnA, selects Cys₂₁ for initial modification, and proceeds to Cys₂₁ remains unclear.

Role of the proposed third Fe site. The combined data indicate that the active cofactor is a mixed-valent Fe(II)Fe(III) species, leaving the role of the third Fe binding site detected by Mössbauer spectroscopy, nTDMS of MbnBChighFe (11), and crystallography unclear. To probe the functional significance of this site, two of its ligands, D208 and H210 (Fig. 1*B*), were individually replaced with serine and the resultant D208S and H210S variants expressed in the presence of 250 μ M Fe. According to ICP-MS measurements, the D208S and H210S variants contained 0.92 \pm 0.084 and 1.17 \pm 0.04 equiv Fe, respectively, slightly less than or comparable to Fe content of MbnBChighFe (also expressed with 250 μ M Fe). The 2.7 Å resolution crystal structure of the H210S variant, obtained using the surface entropy reduction variant expressed at 250 μ M Fe, shows the same coordination environment for Fe1 and Fe2 as the structure obtained from MbnBC expressed in the presence of 250 μ M Fe (Fig. 6*B*), including a bridging sulfate ion, but no density whatsoever for Fe3 (Fig. 8*A*, Fig. S11*D*).

Activity assays were then performed as described for redMbnBC_asc. Both variants were able to modify MbnA. While D208S yielded about half as much product as wildtype MbnBC $_{lowFe}$ (Fig. 8B), the H210S variant was significantly less active (Fig. 8C). Nevertheless, these results indicate that a third Fe ion is not essential for activity. To assess the presence of the active Fe(II)Fe(III) species, both variants were reduced with 2 equiv ascorbate and examined by EPR spectroscopy. Each variant exhibits the $g_{ave} = \sim 1.9$ feature attributed to the S = 1/2 Fe(II)Fe(III) species (Fig. S15). While the D208S spectrum is identical to that of wildtype MbnBC in terms of g-values, the spectrum of H210S at 10 K exhibits unresolved g-values, possibly reflecting the presence of multiple cofactor conformers. It is possible that this substitution disrupts the active site geometry, as evidenced by the EPR spectrum, leading to reduced MbnA modification activity. This perturbation is even more evident in the EPR spectrum of the H210S MbnBC-MbnA complex, which is very different from that of wildtype MbnBC in the presence of MbnA. This substitution likely impairs the ability to properly bind the substrate. These combined findings further support the assignment of a diiron Fe(II)Fe(III) active species.

Mechanistic implications. The identification of the MbnBC active species as a diiron, rather than triiron, cluster adds to an ever-expanding group of enzymes that use nonheme diiron cofactors to activate dioxygen and oxidize substrates (25, 26). There are three major families of nonheme diiron enzymes: (i) the ferritin-like oxidases and oxygenases (FDOs), which include soluble methane monooxygenase (27), ribonucleotide reductase (28), aldehyde deformylating oxygenase (29), and stearoyl-acyl carrier protein desaturase (30), (ii) the recently discovered family of heme-oxygenase-like diiron enzymes (HDOs), and (iii) the mixed-valent diiron oxygenases and oxidases (MVDOs). All FDOs and HDOs studied to date activate O₂ with the Fe₂(II) forms of their cofactors; a two-electron oxidative addition forms a peroxo-Fe₂(III) intermediate, which can either directly transform the substrate or convert to high-valent, substrate-oxidizing intermediates upon O-O cleavage. FDOs and HDOs typically carry out 2e⁻ oxidations of their substrates and require

two additional electrons, which are usually provided by a reduced nicotinamide, to convert the Fe₂(III) "product" of substrate oxidation back to the O₂-reactive Fe₂(II) form.

By contrast, the MVDOs, which include the enzymes myo-inositol dioxygenase (MIOX), PhnZ, and TmpB (15-17) activate O₂ via a one-electron oxidative addition at the Fe(II) of their Fe(II)Fe(III) cofactors, while the Fe(III) site coordinates the substrate. The resultant superoxo-Fe₂(III) intermediate can initiate substrate oxidation by abstraction of hydrogen from a partially activated aliphatic carbon. Importantly, this strategy allows MVDOs to carry out four-electron oxidations of their substrates and not to require a co-substrate. The four-electron oxidation of a cysteine to an oxazolone ring and thioamide amide group by MbnBC is yet another new reaction for this family. Given evidence that the Fe(II)Fe(III) cofactor of MbnBC can interact with its substrate MbnA in the absence of dioxygen, it is likely that the reaction is initiated similarly to the MIOX and PhnZ reactions (Fig. S16) (26). While the Fe(III) ion binds to the cysteine thiol, dioxygen binds to the Fe(II), forming an iron-superoxo intermediate. Then an oxidative cyclization analogous to that in the isopenicillin N synthase (IPNS) mechanism (31) could occur by cleaving the C β -H bond in the cysteine residue to form a β-lactam ring. After C-S desaturation, presumably by a ferryl intermediate, the β-lactam ring would be opened by an enzyme nucleophile followed by formation of a five-membered oxazolone ring (Fig. S16) (26). While these mechanistic steps are speculative, the identification of an Fe(II)Fe(III) cluster as the starting point for the catalytic cycle sets the stage for future spectroscopic and kinetic investigations. Moreover, MbnBC is unique in that it performs the reaction twice on the same substrate, modifying two specific cysteine residues. How MbnBC distinguishes the modifiable cysteines from other cysteines in MbnA and why disruption of Cys₂₁ precludes modification of Cys₂₇ (11) remain open questions.

Materials and Methods

Expression and purification of MbnBC proteins. A construct of $Ms.\ trichosporium\ OB3b\ MbnBC\ that includes the <math>mbnC$ gene with an N-terminal His $_6$ tag and a tobacco etch virus (TEV) cleavage site and the mbnB gene with a C-terminal Strep-II tag was used (11). The D208S and H210S MbnBC variants were generated by site-directed mutagenesis using a QuikChange Lightning kit (Agilent) (Table S2). All three proteins were expressed and purified as reported previously (11) except that the concentration of Fe in the autoinduction growth medium was varied. MbnBC $_{lowFe}$ was expressed with 160 μ M ferrous ammonium sulfate while all other proteins including MbnBC $_{highFe}$, D208S, and H210S were expressed with 250 μ M ferrous ammonium sulfate (MilliporeSigma). 57 Fe-labeled MbnBC was also prepared as described previously (11) except that the concentration of 57 Fe (Isoflex) added to the growth medium was 160 μ M for MbnBC $_{lowFe}$. A buffer containing 25 mM MOPS, pH 7.2, 250 mM NaCl, and 10% glycerol was used for all experiments unless noted.

ICP-MS analysis. ICP-MS experiments were performed at the Quantitative Bio-element Imaging Center at Northwestern University. The samples were digested in concentrated nitric acid (Thermo Fisher Scientific) by incubating at 65 °C for 1 h and then diluted with MilliQ water to a final solution of 3% nitric acid. An element standard containing Fe (Inorganic Ventures) was used to prepare a 100 ng/ml standard solution in 3% nitric acid (vol/vol). Online dilution was carried out by the prepFAST system and used to generate calibration curves consisting of 100, 50, 10, 2, 1, and 0.5 ng/g of Fe. Samples were measured using a Thermo iCAPQ ICP-MS instrument equipped with a CETAC ASX260 autosampler (Thermo Fisher Scientific). The isotopes selected for analysis were ⁵⁶Fe, ⁵⁷Fe, ⁸⁹Y, and ¹¹⁵In (⁸⁹Y and ¹¹⁵In were used as internal standards for data interpolation and machine stability). The data were analyzed using QTEGRA software. All reported values were measured with 3-5 independent protein samples.

Preparation of ⁵⁷Fe-labeled MbnBC_{highFe} and MbnBC_{lowFe} for activity assays, EPR spectroscopy, and Mössbauer spectroscopy. Purified ⁵⁷Fe-labeled MbnBC was either oxidized or reduced for further experiments. For oxMbnBC, samples were incubated with 1.5 equiv of potassium ferricyanide (MilliporeSigma) for 20 min at 4 °C followed by removal of excess potassium ferricyanide using a Superdex 75 size exclusion column. All reduced MbnBC samples were prepared in either a Coy anaerobic chamber or an anoxic chamber (Labmaster, MBraun, Stratham,

USA) using oxMbnBC samples. The reduction titration was performed by adding 0.5, 1, and 2 equiv of sodium ascorbate (Acros Organics) or 2 equiv sodium dithionite (MilliporeSigma) followed by incubation at 4 °C for 20 min. Samples of oxMbnBC, redMbnBC_asc (2 equiv ascorbate) and redMbnBC_dt (2 equiv of dithionite) were used for activity assays and characterization by Mössbauer spectroscopy. Samples of MbnA-bound redMbnBChighFe_asc for EPR and Mössbauer spectroscopic analysis were prepared in the anaerobic chamber, by incubation with 2 equiv of MbnA for 20 min at 4 °C.

Activity assays. Stopped-flow absorption spectroscopy was performed using an Applied Photophysics Ltd. (Leatherhead, UK) SX20 stopped-flow spectrophotometer at 5 °C in an anoxic chamber (Labmaster, MBraun, Stratham, USA). The instrument was set for single-mixing with an optical path length of 1 cm and a photodiode-array (PDA) detector. An anaerobic solution of MbnBC (300 μ M) in purification buffer (25 mM MOPS, pH 7.2, 250 mM NaCl, 10% glycerol) was rapidly mixed with an equal volume of O2-saturated buffer containing MbnA (600 μ M), and 1000 points of absorption spectra were acquired in a logarithmic time scale.

All other activity assays were performed using an Agilent Cary 3500 Compact Peltier UV-vis spectrophotometer. For the comparison between MbnBC $_{lowFe}$ and MbnBC $_{highFe}$ samples, 100 μ M MbnBC (150 μ L) was reduced with 2 equiv sodium ascorbate (Acros Organics) in a Coy anaerobic chamber and transferred into a quartz cuvette. The reaction was initiated by adding 1 μ L of 20 mM MbnA (Bio-Synthesis Inc.) and exposure to air. Spectra were collected every 15 s for 15 min. Activity assays with 57 Fe-labeled MbnBC $_{lowFe}$ to compare different oxidation states and with the D208S and H210S variants were initiated by mixing 80 μ M MbnBC in 120 μ L of deoxygenated buffer with 400 μ M MbnA in 120 μ L aerobic buffer (aerobic buffer was used to provide O₂ for the reaction). The reaction was then monitored for 1 h, collecting spectra with an interval of 15 s.

EPR spectroscopy. Samples of 57 Fe MbnBC_{highFe} used for reductive titrations and investigation of MbnA binding were prepared at a protein concentration of 1 mM. Samples were transferred to custom quartz X-band EPR tubes (Quartz Scientific, Inc., Fairport Harbor, Ohio) and continuous wave X-band EPR spectra were collected on a Magnettech MS5000X spectrometer equipped with an Oxford Instruments ESR-900 continuous flow cryostat and an Oxford Instruments ITC-300 temperature controller. Spin quantification was performed using a spin standard of equine skeletal muscle myoglobin (Mb) (Sigma) coordinated by azide. The low-spin Mb-N₃ standard was quantified using the visible absorption of the Soret band of a control Mb sample without azide (ϵ = 188,000 M-1 cm-1 at 409 nm) (32).

For ⁵⁷Fe-labeled MbnBC_{lowFe}, 0.45 mM protein was used to prepare samples of oxMbnBC_{lowFe}, redMbnBC_{lowFe}_asc, and redMbnBC_{lowFe}_dt. The oxMbnBC_{lowFe} sample (~100 μL) was transferred into a custom quartz Q-band EPR tube and frozen in liquid nitrogen under aerobic conditions, while the two reduced samples were prepared anaerobically in a Coy chamber, transferred to Q-band EPR tubes, and frozen and stored in liquid nitrogen until analysis. X-band EPR measurements were performed on a Bruker ESP-300 spectrometer with a liquid helium flow Oxford Instruments ESR-900 cryostat. All samples were measured using 200 μW of microwave power, 6 G modulation, 10 G/s scan rate, and 320 ms time constant. Spectra were acquired at 3.9 K to optimize the signals from rhombic high spin Fe(III) and at 10-12 K to optimize the signals from Fe(II)/Fe(III) antiferromagnetically coupled species and subsequently scaled to relative intensities to facilitate comparison. Spectra were also subtracted against a spectrum of buffer in order to correct the baseline and to remove the signal of a copper contaminant associated with buffer reagents. Samples of ⁵⁶Fe MbnBC_{highFe} prepared using the same procedures were also utilized to test the effects of different amounts of ascorbate and of MbnA.

Mössbauer spectroscopy. Samples of 57 Fe-labeled oxMbnBC, 57 Fe-labeled redMbnBC_asc, and 57 Fe-labeled redMbnBC_asc with MbnA(300 μL), were prepared at protein concentrations of 1 mM (MbnBC_{highFe}) or 0.9 mM (MbnBC_{lowFe}). Mössbauer spectra were recorded on a spectrometer from SEECO (Edina, MN) equipped with a Janis SVT-400 variable-temperature cryostat. The reported isomer shift is given relative to the centroid of the spectrum of α -iron metal at room temperature. Simulations were carried out using the program WMOSS (SEE Co., Edina, MN).

Crystallization and structure determination. The sequence of wild-type MbnBC from *Ms. trichosporium* OB3b was analyzed by the XtalPred (33) and SERp (18) servers to predict disordered loops and identify high entropy surface patches. Based on the results, 8 residues at the MbnB C-terminus were deleted, and residues comprising two surface patches, MbnB E67, E69, and K70, and MbnC E162, E164, and K165, were identified for mutation to alanine. This construct, with an N-terminal His₆ and SUMO tag, was synthesized and inserted into the pCDFDuet-1 vector (GenScript). Proteins were expressed and purified as described above. The H210S MbnBC variant for crystallization was generated using a QuikChange Lightning kit (Agilent). After the initial purification using Ni-loaded 5 mL HiTrap Chelating column as described previously (11), protein was incubated with SUMO protease overnight at 4 °C with nutation. Cleaved proteins were then purified by loading the entire reaction onto the Ni-loaded 5 mL HiTrap Chelating column followed by washing with two column volumes of 25 mM MOPS, pH 7.2, 250 mM NaCl, 10% glycerol, and 10 mM imidazole, and collection of the flow-through fraction. Further purification was performed using a Superdex 75 size exclusion column.

Before setting up crystal trays, all protein samples were exchanged into 25 mM MOPS, pH 7.2, and 250 mM NaCl. Initial crystals were obtained via sitting drop vapor diffusion at 10 °C overnight using 10 mg/ml protein in 2 µL drops at a 1:1 ratio with a precipitant containing 0.2 M lithium sulfate, 0.1 M Bis-Tris pH 6.5, 25% (w/v) PEG3350 (B11 in MCSGII, Anatrace). All other crystals were grown in similar conditions containing 0.2 M lithium sulfate (Alfa Aesar), 0.1 M Bistris propane pH 7.0 (Hampton Research), and 20-26 % (w/v) PEG3350 (Hampton Research). Crystals were soaked in a cryoprotectant solution containing the crystallization solution with 10% ethylene glycol for 1-3 min and then frozen in liquid nitrogen. Data were collected at 66 K at a wavelength of 1.722 Å at the LS-CAT beamline 21 ID-D at the Advanced Photon Source at Argonne National Laboratory. The crystals belong to space group C2221 with two MbnBC molecules in the asymmetric unit. The data were processed using XDS (34), and the initial structure was solved by Fe SAD using autoSHARP (35). All additional structures were solved by molecular replacement using Phenix (36). Model building and refinement were performing using Coot (37) and Phenix (36). Data collection and refinement statistics are summarized in Table S1.

The interaction with MbnA was modeled using the newly accessible advanced version of ColabFold

(https://colab.research.google.com/github/sokrypton/ColabFold/blob/main/beta/AlphaFold2_adva nced.ipynb) with the following parameters: MbnABC oligomeric ratio of 1:1:1; msa_method jackhmmer; msa_format fas; pair_mode unpaired+paired; pair_cov 50; pair_qid 20; rank_by pTMscore; use_turbo unchecked; num_models 5; use_ptm checked; num_ensemble 1; max_recycles 3; tol 0; is_training unchecked; num_samples 1; subsample_msa checked (21). The first ranked prediction model is presented.

Tandem mass spectrometry. A reaction mixture of redMbnBC_{lowFe} asc with MbnA was analyzed by tandem MS. Prior to analysis, the sample was reduced by the addition of 2 mM DT and incubated at 40 °C for 30 min. UHPLC-HRMS/MS analysis was performed using an Agilent 1290 Infinity II UHPLC System placed in line with a Thermo Q-Exactive mass spectrometer. Analytes were separated on a Kinetex C18 reversed-phase column (50 × 2.1 mm i.d, 1.3 μm particle size; [Phenomenex]) using a flow rate of 0.7 mL/min. The solvent system consisted of solvent A (0.1% formic acid, 5% ACN in H₂O) and solvent B (0.1% formic acid in ACN). Metabolite separation was achieved following a 10 min gradient as follows: 0% to 45% B (0 to 8.4 min), 45% to 100% B (8.4 to 8.8 min), 100% B (8.8 to 9.0 min), and 100% to 0% B (9.0 to 10 min), Electrospray ionization was achieved using an H-ESI source with capillary temperature at 280 °C, sheath gas at 60 units, aux gas at 15 units, and spray voltage at 3.5 kV. In positive polarity mode, MS¹ data were collected at a resolution of 35,000 in a scan range of 200-2000 m/z. Precursors were fragmented in the HCD cell, and MS/MS scans were collected at a resolution of 17,500 using targeted PRM analysis with an isolation window of 2.0 m/z and a range of normalized collision energies between 20-25 units. Spectra were processed using Xcalibur Qualbrowser (Thermo Scientific), deconvoluted using the Xtract algorithm, and analyzed with ProSight Lite (Proteinaceous, Inc). Fragment ions were matched with an error tolerance of 15 ppm.

Data Availability

The atomic coordinates and structure factors have been deposited in the Protein Data Bank with accession numbers 7TCR, 7TCX, 7TCU, and 7TCW. All other study data are included in the article and SI Appendix.

Acknowledgments

This work was supported by NIH grants GM118035 (A.C.R.), F32 GM131665 (Y.P.), T32GM008382 (R.J.J), F32 GM136156 (J.W.S), T32GM008449 (R.M.R), GM127079 (C.K.). GM111097 (B.M.H), P41 GM108569 (N.L.K.), and NSF grants MCB1908587 (B.M.H) and CHE2108583 (C.K. and J.M.B.). ICP-MS analysis was performed at the Northwestern University Quantitative Bio-element Imaging Center generously supported by NASA Ames Research Center Grant NNA04CC36G. This work utilized the LS-CAT beamlines of the Advanced Photon Source, which is a United States Department of Energy (DOE) Office of Science User Facility operated for the DOE Office of Science by Argonne National Laboratory under Contract DE-AC02-06CH11356. Use of LS-CAT Sector 21 was supported by the Michigan Economic Development Corporation and the Michigan Technology Tri-Corridor (Grant 085P1000817). We acknowledge staff and instrumentation support from the Structural Biology Facility at Northwestern University, the Robert H Lurie Comprehensive Cancer Center of Northwestern University and NCI CCSG P30 CA060553. We thank Zdzislaw Wawrzak for assistance with crystallographic data analysis and Dr. Grace Kenney for preparation of the MbnBC D208S and H210S variant plasmids.

References

- 1. G. E. Kenney, A. C. Rosenzweig, Methanobactins: maintaining copper homeostasis in methanotrophs and beyond. *J. Biol. Chem.* **293**, 4606-4615 (2018).
- 2. J. C. Müller, J. Lichtmannegger, H. Zischka, M. Sperling, U. Karst, High spatial resolution LA-ICP-MS demonstrates massive liver copper depletion in Wilson disease rats upon Methanobactin treatment. *J. Trace Elem. Med. Biol.* **49**, 119-127 (2018).
- 3. G. E. Kenney, A. C. Rosenzweig, Chalkophores. Annu. Rev. Biochem. 87, 645-676 (2018).
- 4. G. E. Kenney, A. C. Rosenzweig, Genome mining for methanobactins. *BMC Biol.* **11**, 17 (2013).
- 5. B. D. Krentz *et al.*, A comparison of methanobactins from *Methylosinus trichosporium* OB3b and *Methylocystis* strain SB2 predicts methanobactins are synthesized from diverse peptide precursors modified to create a common core for binding and reducing copper ions. *Biochemistry* **49**, 10117-10130 (2010).
- 6. L. A. Behling *et al.*, NMR, mass spectrometry and chemical evidence reveal a different chemical structure for methanobactin that contains oxazolone rings. *J. Am. Chem. Soc.* **130**, 12604-12605 (2008).
- 7. A. El Ghazouani *et al.*, Variations in methanobactin structure influences copper utilization by methane-oxidizing bacteria. *Proc. Natl. Acad. Sci. USA* **109**, 8400-8404 (2012).
- 8. G. E. Kenney *et al.*, Characterization of methanobactin from *Methylosinus* sp. LW4. *J. Am. Chem. Soc.* **138**, 11124-11127 (2016).
- 9. A. Baslé, A. El Ghazouani, J. Lee, C. Dennison, Insight into metal removal from peptides that sequester copper for methane oxidation. *Chemistry* **24**, 4515-4518 (2018).
- 10. Y. J. Park *et al.*, Characterization of a copper-chelating natural product from the methanotroph *Methylosinus* sp. LW3. *Biochemistry* **60**, 2845-2850 (2021).
- 11. G. E. Kenney et al., The biosynthesis of methanobactin. Science 359, 1411-1416 (2018).
- 12. V. J. DeRose, K. E. Liu, S. J. Lippard, B. M. Hoffman, Investigation of the dinuclear Fe center of methane monooxygenase by advanced paramagnetic resonance techniques: on the geometry of DMSO binding. *J. Am. Chem. Soc.* **118**, 121-134 (1996).
- 13. R. Davydov, A. M. Valentine, S. Komar-Panicucci, B. M. Hoffman, S. J. Lippard, An EPR study of the dinuclear iron site in the soluble methane monooxygenase from *Methylococcus capsulatus* (Bath) reduced by one electron at 77 K: the effects of component interactions

- and the binding of small molecules to the diiron(III) center. *Biochemistry* **38**, 4188-4197 (1999).
- 14. T. M. Makris, M. Chakrabarti, E. Münck, J. D. Lipscomb, A family of diiron monooxygenases catalyzing amino acid beta-hydroxylation in antibiotic biosynthesis. *Proc. Natl. Acad. Sci. USA* **107**, 15391-15396 (2010).
- 15. G. Xing *et al.*, Oxygen activation by a mixed-valent, diiron(II/III) cluster in the glycol cleavage reaction catalyzed by *myo*-inositol oxygenase. *Biochemistry* **45**, 5402-5412 (2006).
- B. Wörsdorfer et al., Organophosphonate-degrading PhnZ reveals an emerging family of HD domain mixed-valent diiron oxygenases. Proc. Natl. Acad. Sci. USA 110, 18874-18879 (2013).
- 17. L. J. Rajkovich *et al.*, A new microbial pathway for organophosphonate degradation catalyzed by two previously misannotated non-heme-iron oxygenases. *Biochemistry* **58**, 1627-1647 (2019).
- 18. L. Goldschmidt, D. R. Cooper, Z. S. Derewenda, D. Eisenberg, Toward rational protein crystallization: A Web server for the design of crystallizable protein variants. *Protein Sci.* **16**, 1569-1576 (2007).
- 19. D. Das *et al.*, The structure of the first representative of Pfam family PF09836 reveals a two-domain organization and suggests involvement in transcriptional regulation. *Acta Crystallogr. Sect F Struct. Biol. Cryst. Commun.* **66**, 1174-1181 (2010).
- 20. J. Jumper *et al.*, Highly accurate protein structure prediction with AlphaFold. *Nature* **596**, 583-589 (2021).
- 21. M. Mirdita et al., ColabFold Making protein folding accessible to all. bioRxiv (2021).
- 22. B. J. Burkhart, G. A. Hudson, K. L. Dunbar, D. A. Mitchell, A prevalent peptide-binding domain guides ribosomal natural product biosynthesis. *Nat. Chem. Biol.* **11**, 564-570 (2015).
- 23. J. R. Chekan, C. Ongpipattanakul, S. K. Nair, Steric complementarity directs sequence promiscuous leader binding in RiPP biosynthesis. *Proc. Natl. Acad. Sci. USA* **116**, 24049-24055 (2019).
- 24. H. J. Kim *et al.*, Methanobactin, a copper-acquisition compound from methane oxidizing bacteria. *Science* **305**, 1612-1615 (2004).
- 25. A. J. Jasniewski, L. Que, Dioxygen activation by nonheme diiron enzymes: diverse dioxygen adducts, high-valent intermediates, and related model complexes. *Chem. Rev.* **118**, 2554-2592 (2018).
- 26. L. J. Rajakovich *et al.*, "5.10 Emerging structural and functional diversity in proteins with dioxygen-reactive dinuclear transition metal cofactors" in Comprehensive Natural Products III, H.-W. Liu, T. P. Begley, Eds. (Elsevier, Oxford, 2020), https://doi.org/10.1016/B978-0-12-409547-2.14864-4, pp. 215-250.
- 27. R. Banerjee, J. C. Jones, J. D. Lipscomb, Soluble methane monooxygenase. *Annu. Rev. Biochem.* **88**, 409-431 (2019).
- 28. J. Stubbe, D. G. Nocera, C. S. Yee, M. C. Chang, Radical initiation in the class I ribonucleotide reductase: long-range proton-coupled electron transfer? *Chem. Rev.* **103**, 2167-2201 (2003).
- 29. C. Krebs, J. M. Bollinger, Jr., S. J. Booker, Cyanobacterial alkane biosynthesis further expands the catalytic repertoire of the ferritin-like 'di-iron-carboxylate' proteins. *Curr. Opin. Chem. Biol.* **15**, 291-303 (2011).
- 30. B. G. Fox, K. S. Lyle, C. E. Rogge, Reactions of the diiron enzyme stearoyl-acyl carrier protein desaturase. *Acc. Chem. Res.* **37**, 421-429 (2004).
- 31. P. L. Roach *et al.*, Structure of isopenicillin *N* synthase complexed with substrate and the mechanism of penicillin formation. *Nature* **387**, 827-830 (1997).
- 32. H. H. Liu, Y. Q. Wan, G. L. Zou, Redox reactions and enzyme-like activities of immobilized myoglobin in aqueous/organic mixtures. *J. Electroanal. Chem.* **594**, 111-117 (2006).
- 33. L. Slabinski *et al.*, XtalPred: a web server for prediction of protein crystallizability. *Bioinformatics* **23**, 3403-3405 (2007).
- 34. W. Kabsch, Integration, scaling, space-group assignment and post-refinement. *Acta Cryst.* **D66**, 133-144 (2010).

- C. Vonrhein, E. Blanc, P. Roversi, G. Bricogne, "Automated structure solution with autoSHARP" in Methods in Molecular Biology, S. Doublié, Ed. (Humana Press, Inc., Totowa, NJ, 2007), vol. 364, pp. 215-230. 35.
- P. D. Adams et al., PHENIX: a comprehensive Python-based system for macromolecular 36. structure solution. *Acta Cryst.* **D66**, 213-221 (2010).
 P. Emsley, B. Lohkamp, W. G. Scott, K. Cowtan, Features and development of Coot. *Acta*
- 37. Cryst. **D66**, 486-501 (2010).

A MbnA: MTVKIAQKKVLPVIGRAAA LCGSCYPCSCM

Fig. 1. Reaction catalyzed by MbnBC and a model for the MbnB Fe binding site. (A) A representative MbnA sequence from *Methylosinus trichosporium* OB3b contains a leader sequence (gray) and a core sequence (underlined). The cysteine residues that are modified are colored in orange. MbnBC performs a four-electron oxidation to generate an oxazolone ring and a thioamide group from each cysteine residue and neighboring carbonyl group. (*B*) The proposed metal binding site in MbnB showing potential diiron and triiron clusters. Disruption of the amino acid ligands labeled in blue significantly diminished activity. Two other residues, D208 and H210 (labeled in purple), are proposed to bind a third Fe ion.

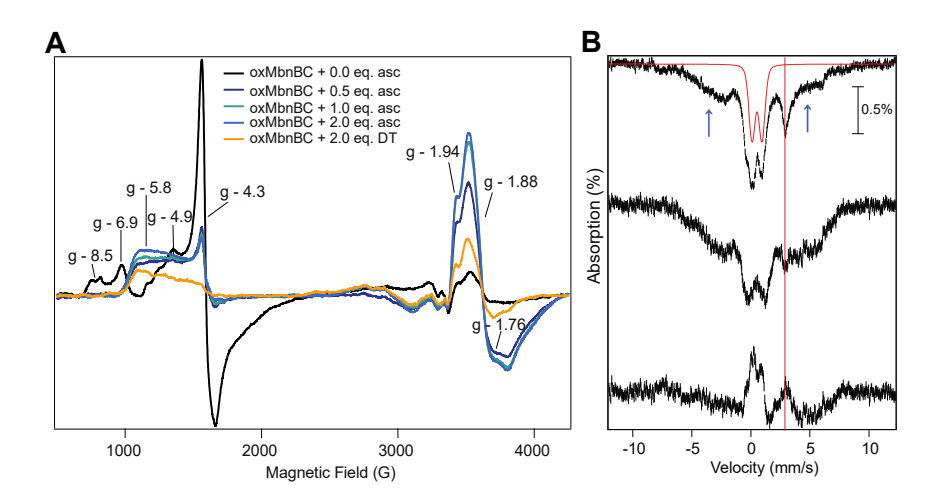


Fig. 2. EPR and Mössbauer spectra of MbnBC. (*A*) EPR spectra of ⁵⁷Fe MbnBC treated with different amounts of ascorbate (asc) and dithionite (DT). (*B*) Mössbauer spectra of oxMbnBC with Fe₂(III) simulation (red) at 20% total Fe signal (top), redMbnBC_asc (middle), and difference spectrum (bottom). Diferric simulation parameters were extracted from previous high-field Mössbauer work (11): Δ Eq = 0.80 mm/s, η = 0.75, and δ = 0.49 mm/s. The red vertical line highlights the high energy line associated with Fe(II) and/or Fe₃(III) species. All samples were prepared with 1 mM ⁵⁷Fe MbnBC and the equiv of reductants was calculated per MbnBC complex.

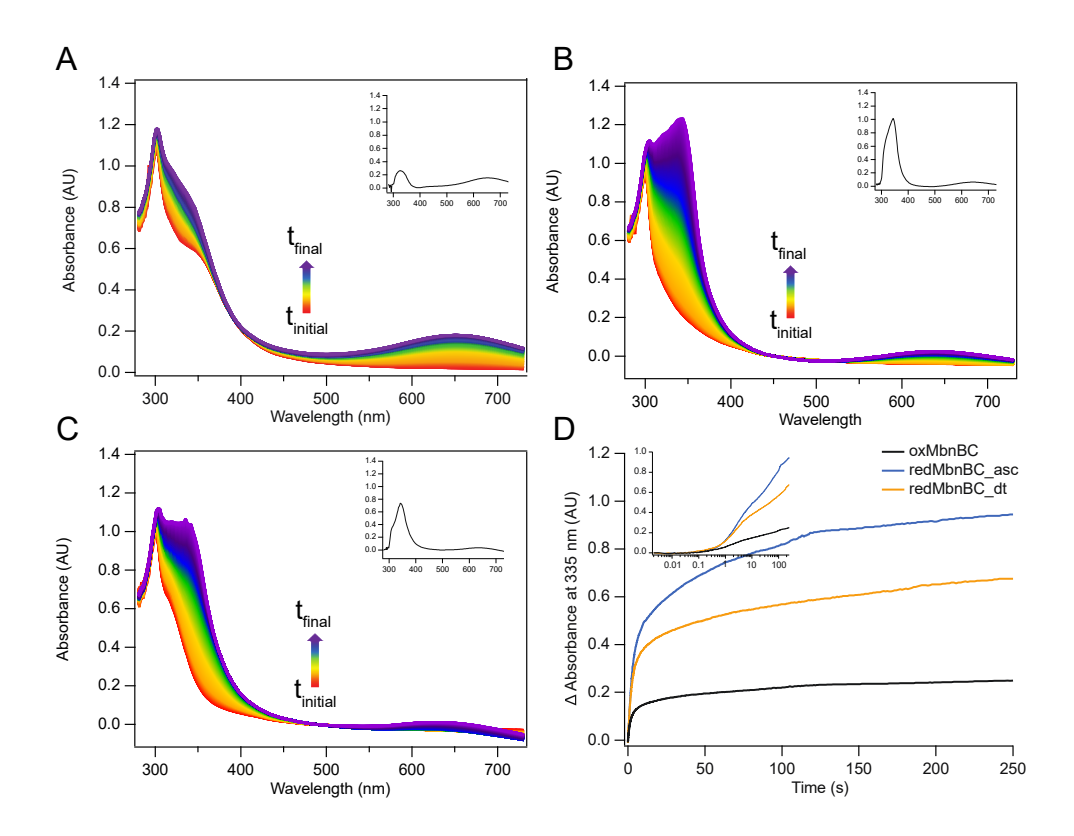


Fig. 3. Reaction of 150 μ M (A) oxMbnBC, (B) redMbnBC_asc, and (C) redMbnBC_dt with 300 μ M MbnA in aerobic buffer using stopped-flow spectroscopy over period of 250 s. Arrows indicate the increase at 335 nm as a function of time with the starting spectrum colored red and the ending spectrum colored purple. Each inset shows the difference spectrum between the initial and final timepoints. (D) Difference absorbance traces at 335 nm attributed to the formation of an oxazolone ring and a thioamide group, obtained by subtracting the absorbance at each point from the initial time point. Inset shows the traces plotted on a log time scale.

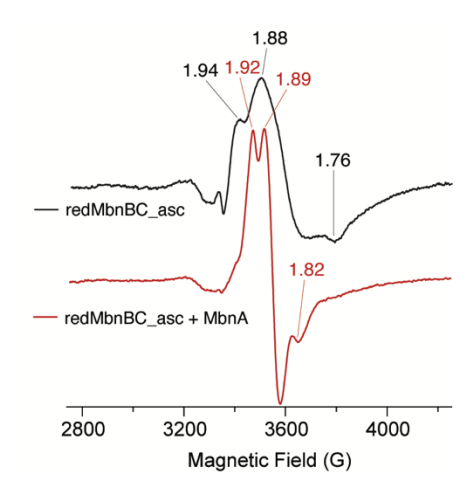


Fig. 4. Effect of MbnA on the EPR spectrum of redMbnBC_asc. Samples were prepared with 1.2 mM redMbnBC_asc and 2 equiv of MbnA per MbnBC complex.

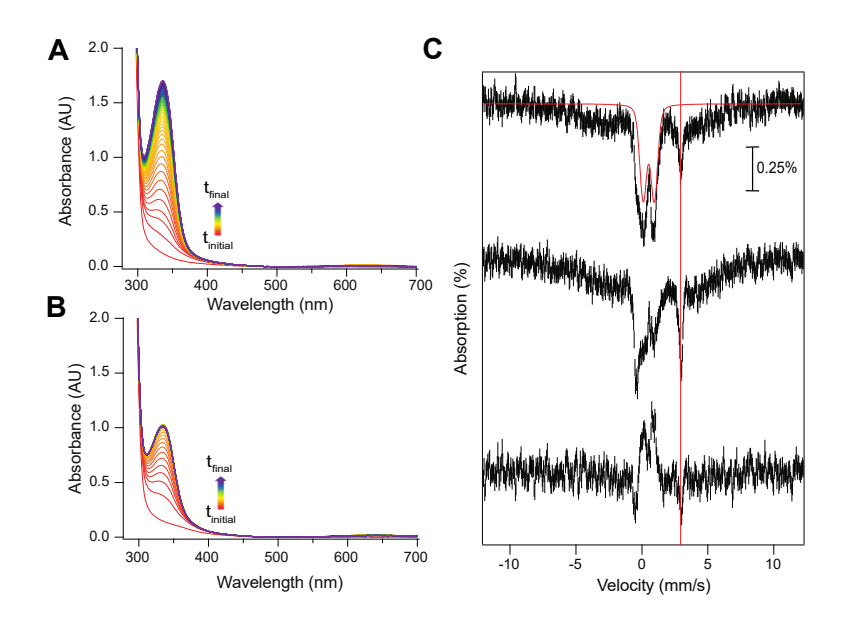


Fig. 5. Activity analysis and Mössbauer spectra of MbnBC produced under low Fe conditions. (A) Activity assay of redMbnBC_{lowFe_}asc. (B) Activity assay of redMbnBC_{highFe_}asc. The reactions were performed by addition of MbnA to a final concentration of 130 μM to a solution of ascorbate-reduced 100 μM MbnBC under aerobic conditions at room temperature. The reaction was monitored every 15 s for a total assay time of 15 min. Arrows indicate the increase at 335 nm as a function of time with the starting spectrum colored red and the ending spectrum colored purple. (C) Mössbauer spectra of oxMbnBC_{lowFe_}(top) with Fe₂(III) simulations (red) at 32% total Fe signal, redMbnBC_{lowFe_}asc (middle), and difference spectrum (bottom). Diferric simulation parameters were extracted from previous high-field Mössbauer work (11): Δ Eq = 0.80 mm/s, η = 0.75, and δ = 0.49 mm/s. The red vertical line highlights the high energy line associated with Fe(II) and/or Fe₃(III) species.

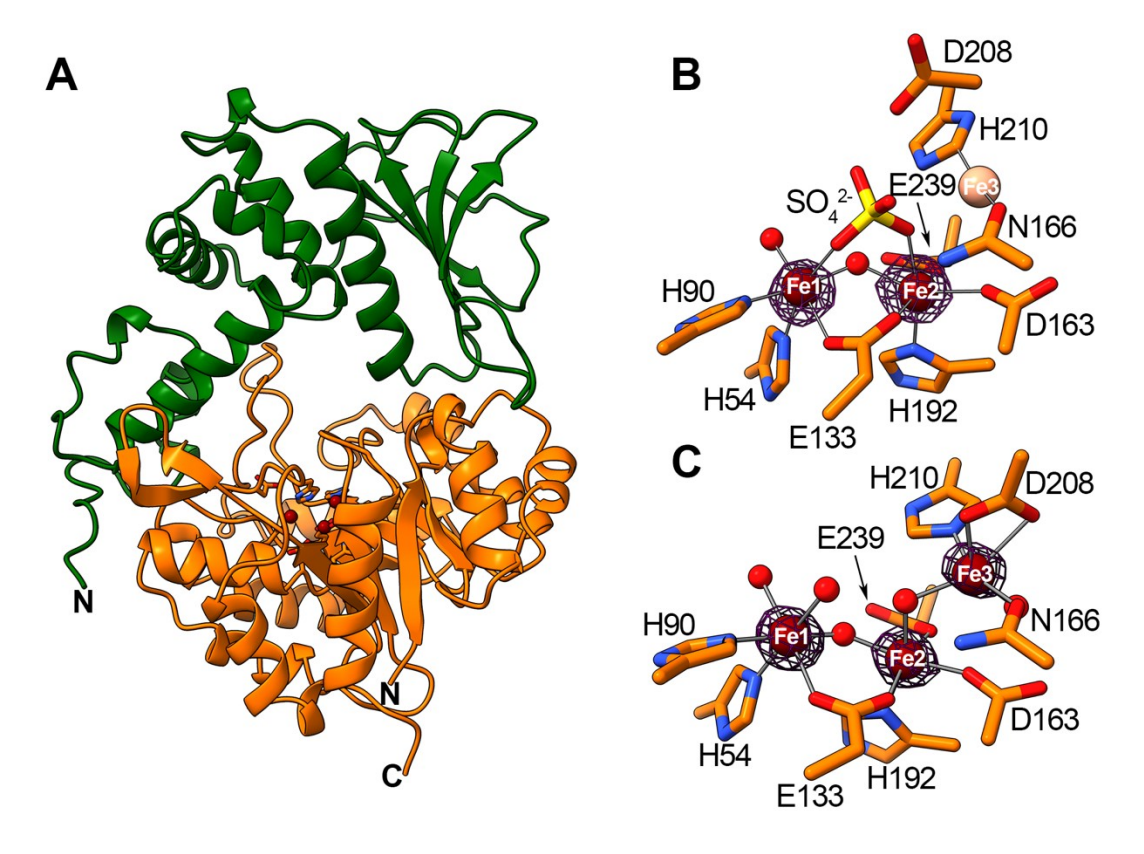


Fig. 6. Crystal structure of *Ms. trichosporium* OB3b MbnBC. (A) Overall structure with MbnB shown in orange and MbnC show in green. The Fe ions in MbnB are shown as dark red spheres and the ligands are shown as sticks. (B) The Fe center in MbnC expressed in the presence of 250 μ M Fe with partially occupied Fe3 site. The Fe anomalous electron density map is superimposed at 25 σ . (B) The Fe center in MbnBC expressed in the presence of 250 μ M Fe and crystallized anaerobically in the presence of the MbnA core peptide with all three Fe sites fully occupied. The Fe anomalous electron density map is superimposed at 20 σ . Solvent molecules are shown as small red spheres.

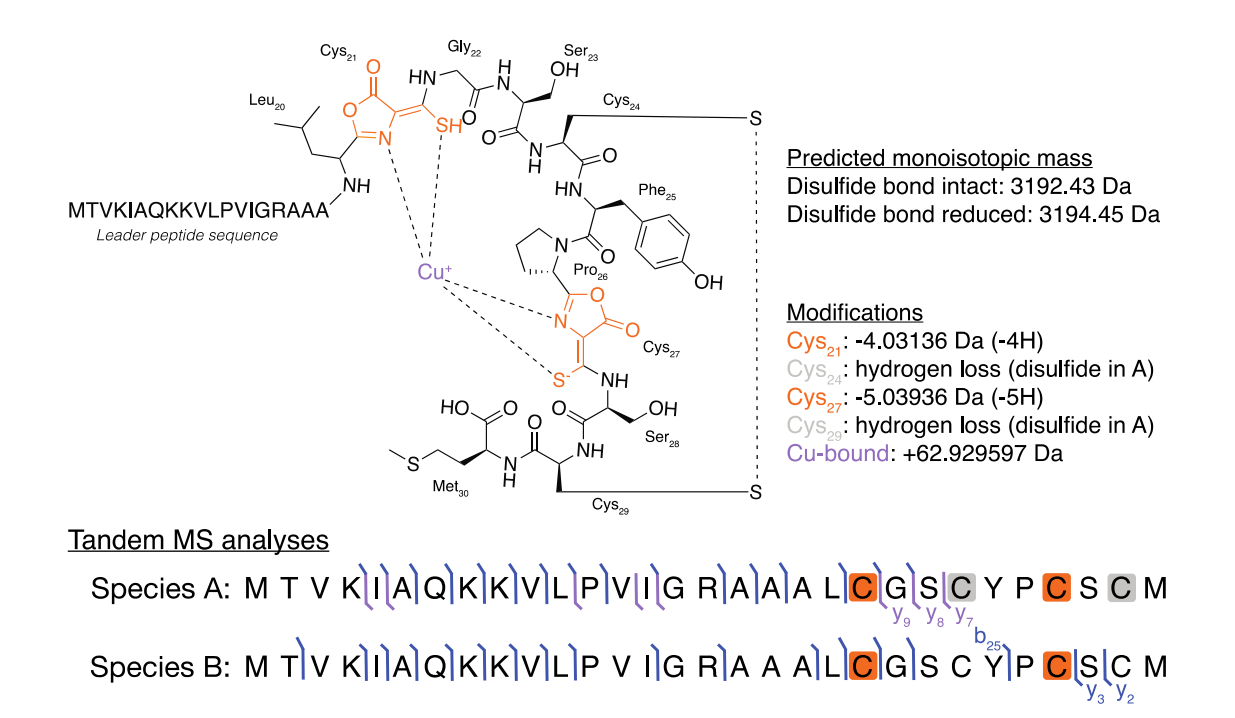


Fig. 7. Mass spectrometric analysis of the product of the optimized MbnBC reaction with MbnA. The reaction mixture contains species A with a disulfide bond and species B in which the disulfide bond is reduced. Cys₂₁ and Cys₂₇ (orange) have each been modified to an oxazolone ring and a thioamide group. Cys₂₄ and Cys₂₉ (gray) form the disulfide bond in species A. All species A y ions colored in purple bind Cu. The y- and b-type ions mentioned in the text are labeled.

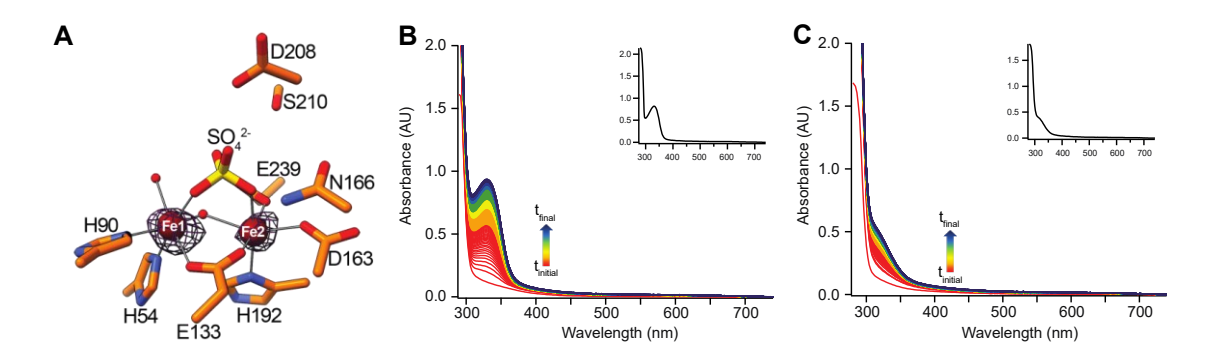


Fig. 8. MbnA modification activity and structure of third Fe site variants. (A) The Fe center in the H210S variant expressed in the presence of 250 μ M Fe. The Fe anomalous electron density map is superimposed at 10σ . For activity assays with (B) D208S and (C) H210S, 40 μ M MbnBC variant was reacted with 200 μ M of MbnA under aerobic conditions. The insets show a difference spectrum between the final and initial time points.